

Research Article

Ambient Zinc K-Edge Extended X-Ray Absorption Fine Structure Studies on Solid Solution Hardening of the $\text{Zn}_{1-x}\text{Be}_x\text{Se}$ Ternary Alloys

Shabina Khan,¹ Javed Mazher,² and Pankaja Singh¹

¹Physics Department, Government Motilal Vigyan Mahavidyalaya, Barkatullah University, Bhopal 462001, India

²Materials Science Program, Addis Ababa University, P.O. Box 1176, Addis Ababa, Ethiopia

Correspondence should be addressed to Shabina Khan; shabinakhank@gmail.com

Received 4 October 2012; Accepted 12 November 2012

Academic Editors: W. A. Badawy, J. Casado, and R. Kudrawiec

Copyright © 2013 Shabina Khan et al. This is an open access article distributed under the Creative Commons Attribution License, which permits unrestricted use, distribution, and reproduction in any medium, provided the original work is properly cited.

Solid solution hardening can be introduced in the zinc selenide by cationic substitution alloying. We are presenting our studies on gradual development of the hardening and the bond-length variations among the heavily Be-doped ternary alloys of $\text{Zn}_{1-x}\text{Be}_x\text{Se}$. These compositionally vivid ternary systems are grown by the Bridgman technique, and a set of careful measurements of synchrotron-based Zn core X-ray absorption spectroscopy are performed on the mixed alloy, which is followed by extraction of useful oscillations of extended X-ray absorption fine structures. A detailed ab initio analysis is also carried out for the mixed alloy's theoretical EXAFS simulations, and suitable data processing codes are used for the subsequent experimental spectra fittings. Various X-ray scattering single and multiple paths around the core atomic environ are simulated and compared with the spectroscopic results. With the aid of as-found parametric values, the hardening and crystalline disorders are discussed and explained in the midst of the multimodal bond-length behaviors and changes induced by the increased alloying amid as-found pseudocrystalline stabilities.

1. Introduction

Group II–VI wide band gap semiconductors are suitable for both long and short wavelength optical devices like tunable blue semiconductor lasers, nanotransistors, and ultrahigh speed and high energy switching devices [1, 2]. Among these semiconductors, the zinc selenide (ZnSe) is highly suitable for deployment in the blue green lasers [3–5]. The ZnSe is a wide band gap semiconductor material and the aptness of the ZnSe mainly lies in its so-called self-activated emission band that is centered at 2.07 eV with the sharp luminescence emission lines owing to its high crystal quality and inherent strain reduction property [1]. Fabrication of the ZnSe laser diode requires high levels of n- and p-type doping in order to obtain the appropriate electrical properties [4]. However, the presence of impurities produces defects mainly from optically active centers, which largely affect any competent luminescence emission. Therefore, early studies of lasing in the ZnSe are limited because the material is not stable enough

to be used in high current or in high excitation regimes [1]. Generation of various point defects in the active region of ZnSe and propagation of the extended defects that mainly originate at interface between the ZnSe and GaAs under working device conditions are some protracted hampering issues in the zinc selenide's commercial deployment [6]. The formation and the propagation of nonradiative defects are limiting factors for the device lifetimes during room-temperature operations. Other noticeable difficulties in the ZnSe lasing devices instigate from iconicity-induced softening of the lattice. A renewed interest in mixed ZnSe -based systems arises after several recent ab initio quantum calculations and experimental studies [7, 8] which predict large covalent bonding between dopant atoms of beryllium and chalcogenide atoms of the mixed crystal and subsequent reduction in overall bond distances, which is a unique observance among the highly ionic II–VI semiconductors. For this reason, the $\text{Zn}_{1-x}\text{Be}_x\text{Se}$ alloys are a new class of II–VI ternary semiconducting compounds that are formed from

the binaries with highly contrasting bond-length properties [7]. Previously, fundamental defects in as grown ZnBeSe (ZBS) materials are studied with a positron spectroscopy and the defects responsible for the photoluminescence decay among the compositionally assorted samples are identified in detail [9]. It is found that the alloy exhibits an unusually large contrast in physical properties manifesting in bond stiffness and bond-lengths distribution of its constituting bonds, leading to a uniquely well-resolved 1-bond-2-mode behavior as already reported in the Raman spectra of this system [10]. From such studies it is well established that various defect dissemination mechanisms in ZnSe are significantly reduced on increasing the lattice rigidity and for the reason that high degree of covalent bonding of Be chalcogenides can lead to an increase of shear modulus in such ternaries [10]. Following this, the mixing of Be chalcogenides with other II–VI binary compounds is a widely accepted procedure for increasing solid solution hardening, and the structural resistance. Thus, the curtailing of the possible defect generation and propagation is one of the major motivating factors for this piece of research.

From Ganguli et al.'s previous studies [11, 12] on the high-pressure EXAFS, we lead to a verdict of pressure dependence of the nearest and the next nearest neighbor distances of Zn (or Be) and Se atoms and pseudo-Debye-Waller factor σ^2 on such binary and ternary systems. However, factors that determine the dependence of these parameters as a function of the alloy composition have not been yet explored fully. In the present set of studies, we tried to address this issue with the help of compositionally dependent wavy fitting of EXAFS equations on the current data sets. The substitution-doped system like ZnBeSe, which is studied in the present work, is a novel system and its EXAFS characterization protocols are not very well developed. Hence, full details of the steps adopted during data processing and subsequent EXAFS analysis are included in the paper. It is also interesting to explore bond-length distributions in terms of composition-induced tetrahedral lattice structural distortions among the ternaries. A pronouncement of accommodation of the solid solution hardening due to the difference in Zn–Se and Be–Se bond lengths is also predominantly expected owing to a probable displacement of Se atoms toward the Be atoms. At this point it is highly desirable to present our groundwork results of the extended X-ray absorption fine structure (EXAFS) measurements at Zn K-edges on the compositionally varied (Zn,Be)Se alloyed samples in ambient conditions at a room pressure to get a better insight into the type of disorders and mechanical deformations both qualitatively and quantitatively.

2. Experimental

A set of compositionally vibrant seven high quality samples (ZnSe, A, B, C, D, E, and F) of the alloy of $Zn_{1-x}Be_xSe$ are prepared by a high pressure horizontal Bridgman technique with Be cationic mass fraction (x) values of 0.00, 0.06, 0.16, 0.27, 0.33, and 0.42, respectively; details of synthesis method are given elsewhere [13, 14]. All the samples are found to acquire ZnS or zinc-blende type of crystal structure. A

powdered mixture of ZnSe of purity $\sim 99.999\%$ and beryllium of purity $\sim 99.8\%$ is used as a crucible charge and the temperature of the heating zone is stabilized to 1850 K. The crucible is moved out of the heating zone at the rate of about 2.4 mm/h. At high temperatures, the beryllium atoms are found to be partially substituting at Zn locations in the host ZnSe lattice, and thus we have obtained a $Zn_{1-x}Be_xSe$ solid solution that shows high degree of crystallinity. We have found large concentrations of the zinc atom at boule ends after every synthesis run, hence, this part is removed and the as-obtained remaining part of the material is crushed and filled in the boule for next run, and thus the growth procedure is repeated several times to obtain better homogeneity of the $Zn_{1-x}Be_xSe$ crystals. Finally, we cut the samples into plates of about 1.5 mm in thickness and the diameter is kept typically around 10 mm during their mechanical polishing. The samples' surface roughness is cross-checked through atomic force microscopic measurements that confirm the presence of AFM morphological homogeneity; typically, the RMS surface roughness values are smaller than 10 nm. Following this, the composition of the as-prepared alloys and their tetrahedral crystal structures are cross-examined using inductively coupled plasma (ICP) atomic emission spectrometry and X-ray diffraction (XRD) methods. The EXAFS experimental setup, the structural analyses routines, and the investigational conditions are kept identical for all of the seven samples. Ambient condition EXAFS experiments are performed on the XAS beamline at atmospheric pressure and room temperature. The XAS beamline facilitates the dispersive EXAFS and, commissioned at the SOLEIL Synchrotron Radiation Facility located at Gif-sur-Yvette, France [15, 16]. The EXAFS experimental set up has only three major ingredients that comprise the X-ray source, the sample holder, and the X-ray detector. High synchrotron photon flux is applied on the samples that are positioned through a piezo-XY stage. The spectrum is recorded by a high speed CCD camera that is used for the detection of the sample transmission. The focusing optics allows a short acquisition time of ~ 2 to 12 ms. A $\sim 40 \mu\text{m}$ spot size of the X-ray beam on the sample is used to ensure a small signal to noise ratio—typically of 10^{-5} . Conversely, in the dispersive EXAFS method, a change of Bragg's incidence along a bent crystal opens an energy range in the reflected beam, and a correlation between the position and the energy of the X-ray is thus exploited by means of a position sensitive detector. For the dispersive measurements, we have adopted a dipole magnet source that presently allows a data in an enlarged energy domain of ~ 1200 eV at 9–13 keV range. A bending magnet is used advantageously for deficiency of any coherency in the dispersion plane. A 1.2 m long Ir and Rh bent mirror is placed just after the bending magnet source and a second mirror that is 20 cm long placed just before the monochromator (Si-311) in Bragg geometry for rapid focus adjustment. A resolving power ($E/\Delta E$) is found to be 3×10^4 for the Si-311 and 0.7×10^4 for the Si-111. The beamline optics is also capable of adjusting the X-ray focus size of $40 \mu\text{m} \times 40 \mu\text{m}$ in its full width half maxima. Throughout our measurements, we have kept the detection mode in a transmission style by using the

charge coupled device (CCD) camera. Throughout the sample measurement the temperature is not taken as a variable parameter; it remains constant. Thus, the temperature-related disorder would also remain constant for all of the samples during the measurements.

Open source EXAFS analyses code IFEFFIT version 0.102.10 [17] is used for the theoretical fitting of the EXAFS k-oscillations and their Fourier transforms. An evenly spaced k-grid (0.05 \AA^{-1}) is used for fitting the oscillations along with the polarization, local field, and core-hole corrections. The fixed data ranges are 3 \AA^{-1} – 15 \AA^{-1} and 1 \AA – 6 \AA for the processed k-oscillations and their FTs respectively. The EXAFS fitting parameters are Debye-Waller factor σ^2 , change in the radial distances from the core Zn atom (ΔL), amplitude correction factor S_0^2 , and absorption edge energy shift ΔE_0 from the theoretical value of the edge (9.562 keV), and also we have increased the second shell beryllium-related path degeneracies with increasing values of “x.”

3. Results and Discussion

The EXAFS is accredited as a precise method for local structural characterization [18]. It provides information on the atomic structure around any specific atom, which is the Zn core atom in our experiments. Besides, the Zn core’s K edge EXAFS contains information about its near-neighbor atom distances and fluctuations in the corresponding binary or ternary bond lengths. From typical nontruncated raw EXAFS plots, it is very difficult to extract any useful information. The Athena software [17] is used for the preprocessing of the spectrum to obtain the correct bonding lengths from the scattering path distances in various coordination shells around the Zn core and its nearby atoms; this also ensures the exact chemical valance of the Zn.

The truncated EXAFS absorption spectrum represents only the true oscillatory parts of the total XAS spectrum. Higher order sample crystallinity implies less bond-length inhomogeneity, and thus only few kinds of oscillations are observed corresponding to the respective bonds [18, 19]. Spectral positions of these vacillations are also fairly well located with very little variations in their respective oscillatory profiles. It is also previously reported that among low crystalline order materials, the EXAFS spectra usually demonstrated large extent of disparities in the spectral positions of various oscillatory peaks [18]. On plotting the absorption coefficient as a function of E as shown in Figure 1, an overall decrease in the X-ray absorption with increasing energy is clearly noticeable. This feature is accompanied with the presence of a sharp rise in the absorption intensity at the energy corresponding to the Zn K-edge that almost gives a step-like absorption function (μ) at an augmentation of around 9659 eV exhibiting high rates of the optical transition and thus a high quality of the alloy crystal. At the same time, the near edge structures with an approximate width of 100 eV are also noticeable just after the edge position. We have obtained a clear series of wiggles for the EXAFS oscillatory structures that clearly modulates the $\text{Zn}_{1-x}\text{Be}_x\text{Se}$ absorption pattern. This is possible owing to the high sample quality.

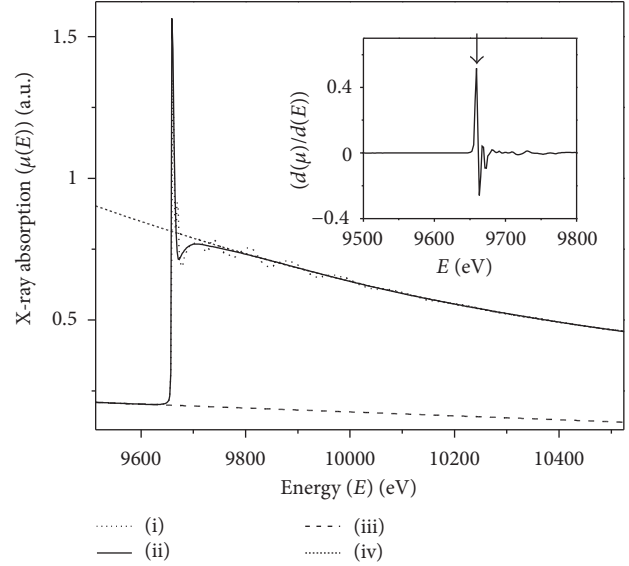


FIGURE 1: Zn K-edge X-ray absorption spectrum (XAS) for the $\text{Zn}_{1-x}\text{Be}_x\text{Se}$ sample (B). The data is processed by using pre edge and postedge lines and a spline-fitted background subtraction. (i) Experimental data is represented by a dotted curve, (ii) smooth continuous runner over the experimental data is the spline background fit, (iii) the bottom pre edge is marked by the dashed line, and (iv) the top post edge is marked by the dashed-dotted line. The inset is a derivative of the absorption and the maximum of the derivative is indicated by the arrow mark, depicting the exact position of the K-edge.

The origin of the wiggle pattern can be attributed to the well-understood quantum mechanical transitions governed by the Fermi golden rule [19]. Hence, the oscillatory part definitely contains detailed structural information of our mixed semiconducting alloy, such as interatomic distances amongst the constituents of Zn, Se, and Be and their respective coordination numbers. Followed by the truncation, the EXAFS spectrum is preprocessed through its normalization. For the purpose of any apposite comparison amongst the spectra measured for varying compositional environment around the core (Zn), the normalization is a prerequisite. Lastly, by subtracting the spectra from the suitable background function $m_0(E)$ above a given absorption edge, which is a smoothly varying atomic background absorption, the preprocessing has been completed.

It is clearly observable from Figure 1 that the XAS data is very well aligned by the use of various Athena preprocessing treads like the preedge and the postedge estimation, the ruling of E_0 , the background removal, and the normalization. Amid the inset of Figure 1, the top baseline that starts just after the attainment of a maximum absorption is the post edge line, while the bottom baseline of the absorption curve which typically covers all data points before the absorption edge represents the pre edge line. Data processing algorithm of the code first pursues a removal of the baseline absorption followed by a calculation of the normalized $\mu(E)$ to ensure that it has no less than two values; one below the absorption

edge and another well above the absorption edge. In addition, an estimate of the edge position E_0 is often made in between these points. The pre edge subtraction from a given input spectrum is further followed by a utilization of a background clearance that uses the Cromer-Liebermann calculations [20] for the post edge background subtraction. The pre edge is further used to find E_0 from maxima of a first derivative absorption to give a reasonable estimate of the threshold energy value E_0 . However, there is no priori criterion for the E_0 's determination and the problem becomes impossible to tackle when the unknown systems have constituent species of different valences and ionicities. Nevertheless, in such cases there is no other option except to consider shift ΔE itself as a variable parameter to the complete fitting procedure and it has to be adjusted with great obscurity. Fortunately, in our present set of analysis the E_0 is a flat parameter. In unison to this, the maximum of a first derivative of the absorption curve is repeatedly compared with the earlier reported results [20] to mark the legitimacy of our investigations, and we have found all the edge positions to be accurate within percentage errors of values lesser than 0.1%. This can be especially important in the case of $\text{Zn}_{1-x}\text{Be}_x\text{Se}$ system's EXAFS analysis where we have attempted to compare many data sets obtained from the dispersive beamline, and the maxima of the first derivative may move by a point or two even for a good EXAFS measurement. Next, the normalization is completed by matching a polynomial function to the post edge absorption data, then extrapolating this function to E_0 . The difference between this value and the extrapolation of the pre edge line to E_0 gives us the true edge step. This is also illustrated in Figure 1 that shows the pre edge line from a quadratic polynomial for the post edge normalization curve and a proper edge step. Hence, the required normalization factor arises from the net increase in the total atomic background absorption at the edge. In practice, the normalization factor is often approximated by a magnitude of the jump in the absorption at the Zn K-edge that is typically of a value of 0.8 absorption units in our spectroscopic measurements. The error in this approximation can be accounted by a small ($\sim 10\%$) correction to the EXAFS Debye-Waller factor, which is sometimes also called a McMaster correction [21].

Figure 2 shows a typical EXAFS modulation with a corrected E_0 for the respective $\text{Zn}_{1-x}\text{Be}_x\text{Se}$ samples (A to E) after normalization and background subtraction taken in the energy range of 9500 eV to 11500 eV for the highly oriented crystalline powder of $\text{Zn}_{1-x}\text{Be}_x\text{Se}$ at 300 K. Through the use of several variants of autobackground utility, the eminence of the EXAFS enhances incredibly and it is reflected by as shown proper alignment of the Zn K-edge position. As evidenced from the spectra (Figure 2), some weak oscillatory wiggles beyond about 30 eV above the absorption edge are obvious. As noted beforehand, these fine structures contain precise information about the local atomic structure around the atom that absorbed the X-rays. In contrast, the region closer to an edge is often dominated by strong scattering processes as well as local atomic resonances in the X-ray absorption and is generally not as readily interpreted as EXAFS. Hence, these near edge resonant signatures are commonly referred to as X-ray absorption near edge structure (XANES) and are

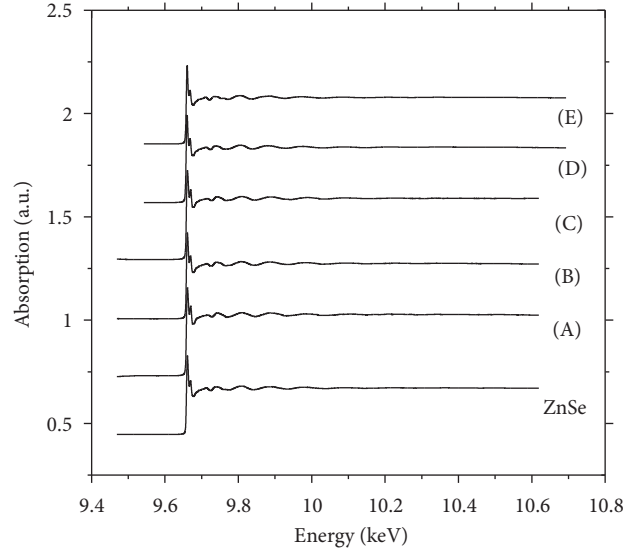


FIGURE 2: The normalized Zn K-edge EXAFS absorption data for the $\text{Zn}_{1-x}\text{Be}_x\text{Se}$ ternary alloy samples with the composition (x) values of 0.0 (ZnSe), 0.06 (A), 0.16 (B), 0.27 (C), 0.33 (D), and 0.42 (E). The spectra are processed by using pre edge and post edge lines and spline-fitted background subtraction, as depicted before in Figure 1.

excluded from the fine structures. Nevertheless, our interest is only in the fine structures that arise owing to single and multiple scatterings from atoms adjoining to the core and lying in the spectral regime of several hundreds of eV above the XANES region [21]. Hence, we have totally neglected the near edge structures in our spectroscopic analysis. As shown among all the spectra of Figure 2, the modulations above the K edge and below the 10.7 keV energies are the EXAFS signals, undoubtedly originated from the contributions of several shells of neighboring atoms and their additions.

The next step is to convert the absorption from $\chi(\mu)$ to $\chi(k)$ by further removing the smooth background from the B-spline fit and using the relation, $\delta k = \delta E / 3.9038 \sqrt{E - E_0}$. In Figure 3, the EXAFS spectra in k -space for the samples A to E are shown. The k spectrum is presented after the proper weighing of k by using an exponent S (S , being 1, 2, 3, ...). We have found a pronounced effect of the k^S weighing on the EXAFS oscillations as they become more uniformly distributed over the given data range along with the suppression of the larger amplitude oscillations from dominating the smaller ones. The frequency dependence of the amplitude, which is also demonstrated from the EXAFS equation is given by $\chi(k) = [\mu(k) - \mu_0(k)] / \mu_0(k) = \sum_j (N_j / k R_j^2) A_j(k) \sin[2kR_j + \psi_j(k)]$ where N_j is the number of atoms at distance R_j in an atomic shell (j), $\chi(k)$ is an oscillatory component of the absorption after subtracting out a smoothly varying atomic contribution $\mu_0(k)$, and $A(k)$ is the amplitude factor that can be further broken down to give a relation $A_j(k) \propto |f_j(k, \pi)| \exp(-2\sigma^2 k^2) \exp(-2R_j / \lambda)$. Furthermore, the $f_j(k, \pi)$ is the atomic backscattering factor for the photoelectron with wave number k , and it depends on the atomic number of the scatterer. Moreover, the EXAFS

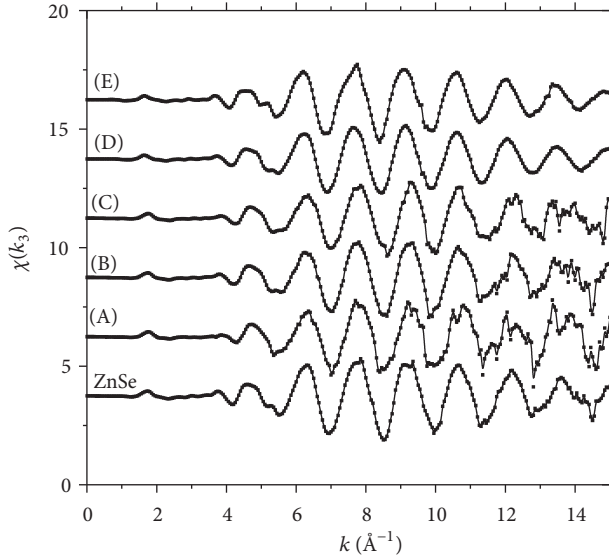


FIGURE 3: The Zn K-edge EXAFS absorption [$\chi(k_3)$] for the $Zn_{1-x}Be_xSe$ samples (A to E) plotted in k -space along with a pure ZnSe spectra. The spectra are arranged vertically upward in increasing order of the Be concentrations and the bottommost is the ZnSe EXAFS.

Debye-Waller factor of σ^2 describes the degree of randomness of the sample crystallinity and is calculated from the mean squared variation of the radial positions of the atoms about their average due to either structural disorder or thermal vibration. Naturally, the overall amplitude of the fine structure of a particular shell enhances in correspondence with the higher coordination (N) and at small distances (R) from the absorbing atom. Typically, we have found a $1/R^2$ type of spherical wave decay in the amplitude maximum with the intershell distances. Besides there is also slowly varying photon energy dependence of the order $1/k$. Likewise, the k_3 weighting becomes imperative to assure that chemical effects on the EXAFS information that are most significant at small k are effectively canceled out [19, 21].

For further analysis in real space we can effectively shield the undesired k -space oscillations by using an appropriate window with its apposite envelop that is casing only the desired oscillations. The Fourier transforms in IFFEFIT first convert the k -space data to real-space [$\chi(r)$] and the back FT for the as-selected radial distances again provides back the spectrum in the filtered k -space ($\chi[q]$). Figures 4(a) and 4(b) represent the real and imaginary parts of the FTs. The curves are generated by interpolating the nonuniformly spaced data onto a uniformly spaced k mesh and are extending to a range of $k = 0$ to $k = 15 \text{ \AA}^{-1}$. The extended data are then Fourier transformed using a fast Fourier transform algorithm [21]. Nonetheless, a relative significance is only of the upper envelop of the combined real and imaginary parts of the FT. The enveloped oscillations are shown in Figure 4(c) as the magnitude of the FT ($\text{mag } \chi[r]$). The centre of the magnitude shows position of the relative bond length in the R -space and the peak profile indicates towards possible distribution

in the bond. The first peak always corresponds for first shell distances and so on [18]. Although absolute values of the transform are found to peak at a distance shifted from the known values by several tenths of angstroms, a correction for these shifts is performed by using systems with known distances; thus one can extract Zn–Se/Be–Se/Zn–Zn/Se–Se lengths. The peak value of the FT also depends on factors such as the weighting of the data, the choice of the threshold energy E , and the phase shift, which are largely responsible for the shifted FT peaks. We have obtained a constant difference between the peak in R and the neighbor distance which is typically -0.45 \AA that is implicitly due to a scattering-related phase shift [$\phi(k)$]. Therefore, the relative amplitude peak shifts [$A(k)$] are taken for the purpose of the comparison of compositional variations. Besides during the steps of both forward and backward Fourier transforms, an isolation of the contributions of the different shells of neighbors is performed and thus each shell is studied separately. In Figure 4(c), the first peak that is positioned at $\sim 2.2 \text{ \AA}$ is the contribution from the first shell comprising the four Se neighbors around the Zn core. The second peak which is observable in Figure 4(c) at the R value of $\sim 3.4 \text{ \AA}$ is due to the contribution of the Be and Zn atoms of the second shell. We have observed a systematic displacement pattern among the second peak positions in the R -space that displaces in the range of 3.2 to 3.5 \AA due to manifestations of Zn–(Be, Se) multibond-length behaviors [11, 12].

The procedure of isolation of contributions from the first, second, and higher shells from the as-obtained $Zn_{1-x}Be_xSe$ EXAFS oscillations in our analysis is achieved by using a suitable envelop or window subsequently over the desired peak of the corresponding shell in the real-space Fourier transformed spectra. This is followed by back FT through the selected windowed part of the spectra only. The envelop line in Figure 4(c) over the first FT peak in real-space curve is a smooth filter window function for isolating the first shell EXAFS. Although as shown the filter is applied to the magnitude of the forward transform, in fact both the real and imaginary parts of the Fourier spectrum are filtered identically, so that a phase error is minimized. The essential feature of a good filter window function is that it does not produce gross distortions in the $Zn_{1-x}Be_xSe$ EXAFS data. After filtering, the back FT is performed to give the oscillatory part corresponding to the first shell as shown in Figure 5 in which the fine structure $\chi(q)$ is plotted as a function of q . The only difference between k and q is that the real space is limited and separately selected for different atomic shells in the q -space; otherwise in principle both are the k -spaces. From the Figure 5 we can wind up some important aspects of EXAFS; firstly we note the absence of all higher frequency variations and noise because the contributions from the second and subsequent higher shells are clearly removed. It is clear from Figure 5 that major contributions in the ZnBeSe's EXAFS oscillation arise from the first shell only, which is manifested from the $\chi(q)$ amplitudes that are almost comparable among Figures 3 and 5. Nonetheless, both the data are plotted in the spaces of k and q , respectively. However, it should be noted that some amount of distortion is unavoidable in the Fourier filtering process which is typically more flying for the first

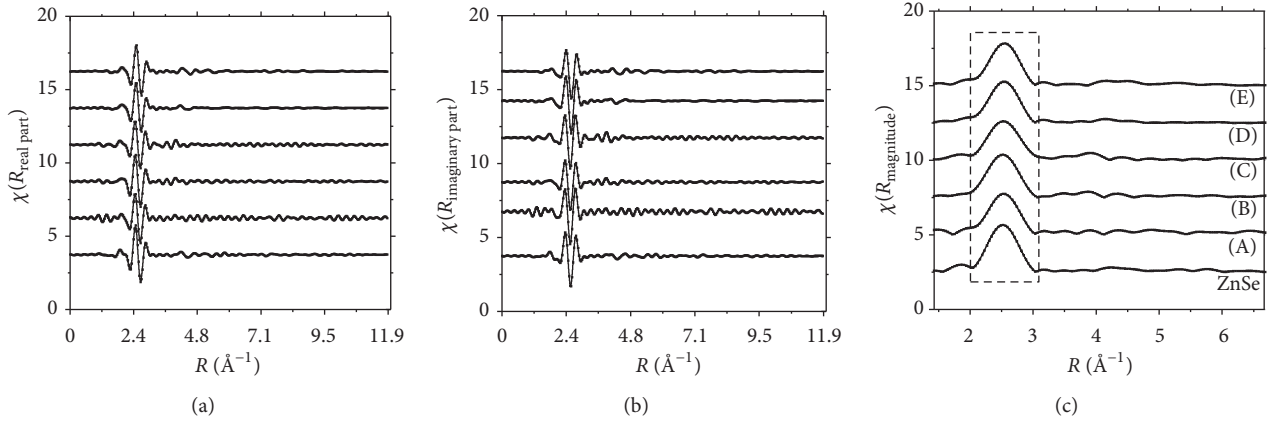


FIGURE 4: (a) Fourier transformed EXAFS plots of Zn K-edge EXAFS absorption data for a binary sample of ZnSe and ternary samples of $\text{Zn}_{1-x}\text{Be}_x\text{Se}$ from A to E plotted in the real space and corresponding to the real part of oscillations $\text{Re}[\chi(r)]$ from the first two shell contributions. (b) EXAFS plots are shown in FT real space, corresponding to the imaginary part of oscillations $\text{Im}[\chi(r)]$ from the first two shell contributions for the various corresponding compositions. (c) Magnitude profile of the Zn K-edge EXAFS absorption data for samples A–E is plotted in the real-space corresponding to the combined envelope overlap of the real and the imaginary parts. The function $\text{Mag}[\chi(r)]$ roughly corresponds to the shape of the amplitude function $A(r)$ and can be produced by FT magnitude filtering of the Zn K-edge $\text{Zn}_{1-x}\text{Be}_x\text{Se}$ for samples A to E. A dotted box indicates the approximate position of the envelope/window over the R magnitude that is used for back FT for the first shell.

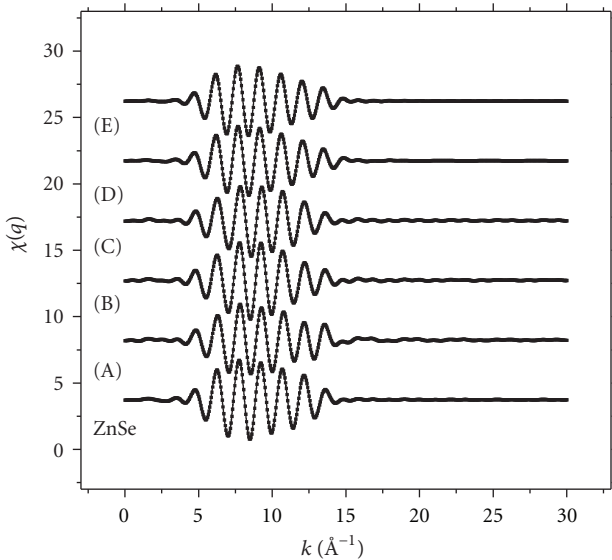


FIGURE 5: Absorption oscillatory variations $[\chi(q_3)]$ for first shell contributions from Zn K-edge EXAFS absorption data are plotted in k -space for $\text{Zn}_{1-x}\text{Be}_x\text{Se}$ samples of composition (x) values of 0.0, 0.06, 0.16, 0.27, 0.33, and 0.42. The oscillations are extracted by using the window filter on the magnitude of the positively enveloped amplitude function $A(r)$ as shown before in Figure 4(c) with the help of a dotted box type window, that is followed by the back FT.

and last oscillations in k due to the application of filtering windows.

In Figure 6(a) the EXAFS fit is plotted as a smooth runner against the experimental encircled data points of the $\chi(k_3)$ EXAFS data for sample A. Figure 6(b) corresponds to the fit in real space and to the EXAFS oscillatory contributions $\chi(q_3)$

from the first shell plotted in q -space and from Figure 6(c) depicts the IFEFFIT calculated various single and multiple scattering paths. Here, the fitting-spaces considered are k , R , and q transformations along with various FT parameters and phase shifts. The used path parameters carry the information of weightings of various fixed variables of the EXAFS equation that includes amplitude correction S_0^2 , EXAFS debye-waller factor σ^2 , and change in the path distances ΔL . An EXAFS path, on the other hand, represents a set of atoms through which the photoelectron scatters before returning to the central atom. The total EXAFS is then just a sum of these individual paths. Using IFEFFIT, we have calculated the single scattering path distances for the near-neighbor (NN) and the next nearest neighbor (NNN) atomic coordination shells from the best-fitted EXAFS spectra. The theoretical curve plotted as continuous runner in Figures 6(a) and 6(b) shows the perfect overlap of the experimental EXAFS oscillation with the tetrahedrally symmetrical $\text{Zn}_{1-x}\text{Be}_x\text{Se}$ system with that of its IFEFFIT theory having high values of the goodness of fit. We have carried the similar analysis for the different compositions with the value of x changes from 0.06 to 0.42 in the data set undertaken for analysis. Figure 6(c) shows the single scattering paths for NN and NNN co-ordinations, and the oscillations $[\chi(q)]$ are plotted in the q -space. The top two spectra of Figure 6(c) are the back FTs of the second shell corresponding to the NNN distances from the Zn and Be atomic co-ordinations. A collective effect of the second shell atoms is also clearly visible in the form of the second NNN peak of Figure 6(b). The lowest spectrum in Figure 6(c) corresponds to the best theoretical fit with the experimental data. The change in single scattering NN distance at the Zn K-edge in $\text{Zn}_{1-x}\text{Be}_x\text{Se}$ system roughly corresponds to the change in the bond-length (Zn–Se) and is depicted by the

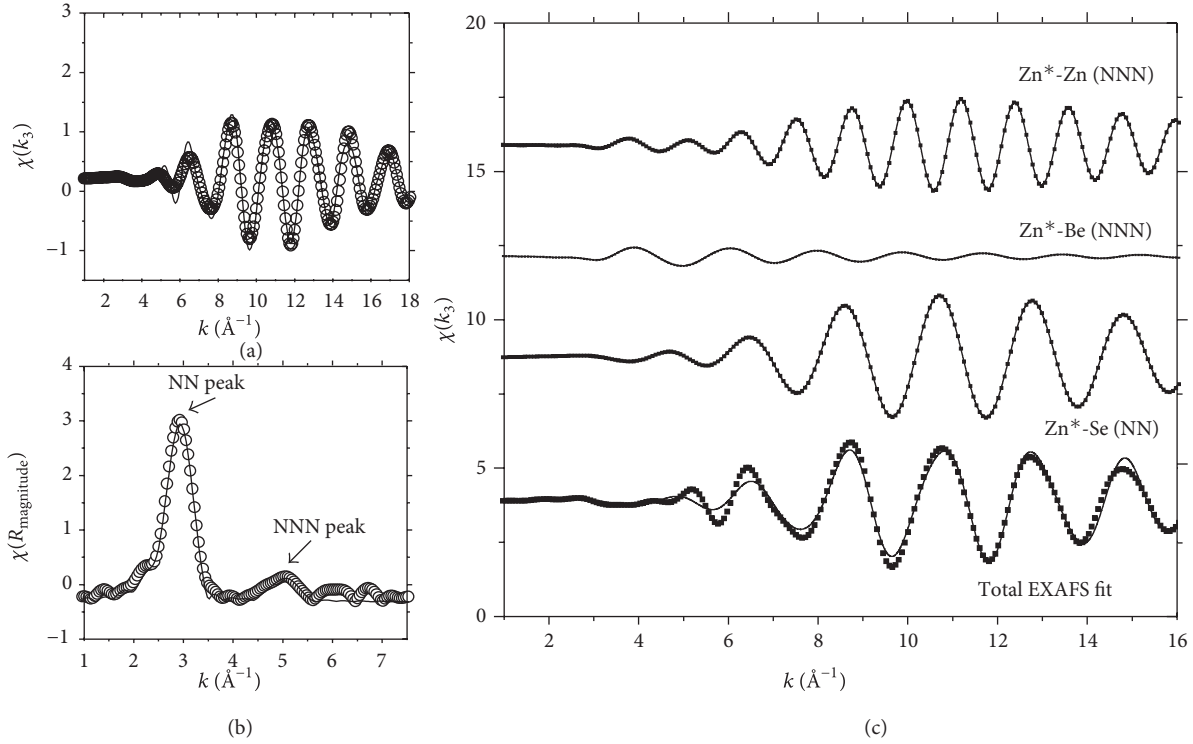


FIGURE 6: (a) The total IFEFFIT fitting of the Zn K-edge EXAFS absorption data for $Zn_{1-x}Be_xSe$ for $x = 0.06$ (sample A) plotted in k -space, $\chi(k_3)$. (b) Total IFEFFIT fitting of Zn K-edge EXAFS absorption data for the sample plotted in real-space $\chi(r)$ amplitude radial distributions, which are clearly discernible for first and second shell scattering paths. (c) Extracted oscillatory contributions of different NN and NNN scattering paths from the Zn K-edge EXAFS absorption plotted in the k -space.

first peak in Figure 6(b). By making a comparison among these two NNN spectra it is evident that the contribution from the Zn coordination is much greater compared to that of Be coordination, which is obvious because of the heaviness of Zn atom and the less concentration of Be in this sample, which is only $x = 0.06$. The mentioned fact is also reflected from intensities of χ peaks in both of these upper spectra; the Zn^*-Be (NNN) distance as depicted from the as-fitted χ intensity peak position is much smaller as compared to that of the NNN distances of Zn^*-Zn in the topmost spectrum. Hence, we have found that only one path in the NNN single scattering events is dominant than the remaining NNN paths. Besides it is clear from the upper two spectra of Figure 6(c), that the k -space oscillation maxima shifted in Zn^*-Be scattering path to the left hand side in comparison to the NNN distance position of the $Zn-Zn$ scattering path. This fact implicates the smaller values of Be-Be bond lengths in contrast to that of Zn-Se bond lengths. Hence in this mixed crystal we have observed two modes in the cation-cation bond-length distribution one for the host cationic species and the other for the cationic dopants.

Even so, we have found that for the first shell, that is, the NN distances, the high goodness of fit is achieved for all the samples. Nonetheless, the data quality does not allow us to go for further NNNN radial peak fitting in real space, which is feasible only when the EXAFS measurements are taken at low temperatures [22]. The corresponding radial distribution

functions of the NN distance in the Zn-Se single scattering paths are calculated for all the assorted compositions. It is expected that at higher Be doping levels, the second shell environment becomes more vivid comprising both the Be and Zn atoms. For instance, the coordination occupancy of Be atom is expected to be four in comparison to the value of zinc occupancy of nine in the sample $Zn_{0.73}Be_{0.27}Se$. Hence it is much easier to analyse first co-ordination shell around the Zn core in relation to its second atomic shell. Nevertheless, still the Zn^*-Se single scattering is the main contributor to the total EXAFS intensity. Also, the disorder and hardening are found to increase in this alloy composition, as evident from the shift as well as increased broadening of the NN radial peaks.

Amongst all the alloy compositions, we have obtained the strongest and most dependable EXAFS signals only from the scattering events for the first co-ordination shell's path (Zn^*-Se). Therefore, we have attempted a systematic comparison of the composition dependent shifts in the radial positions and the corresponding peak broadening for this path. Full width and half maxima (FWHM) is an effective measure of the broadening in the respective EXAFS extracted radial distributions ($g(r)$) as a function of composition (x) of the alloy. It is to be noted that the positional shifts in the ($g(r)$) can be easily ascribed to the compositional change in the Zn-Se bond lengths (ΔL) in present analyses at least for the first shell EXAFS. Similarly, the compositional change

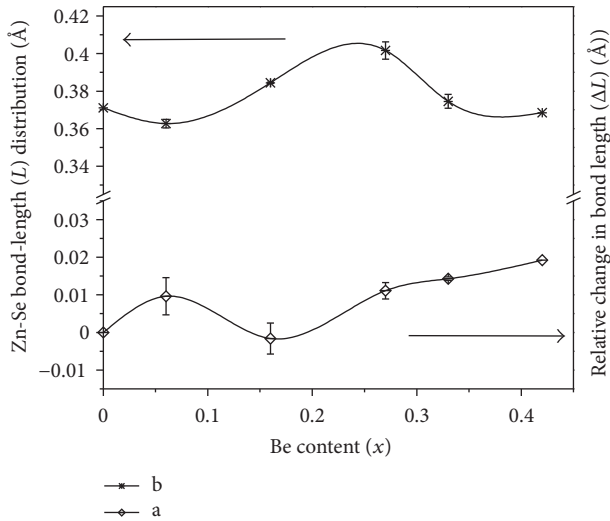


FIGURE 7: (a) A difference of NN distance (Zn–Se bond length) in the ternary alloy with respect to Be content (x) and the equilibrium Zn–Se bond value in strain free binary crystal (2.58 Å) is plotted in a bottom curve. Positive values of ΔL indicate decrease in average Zn–Se bond lengths with the corresponding solid solution hardening induced by increasing the Be concentrations. (b) Zn–Se bond-length (L) distributions calculated from the disorder obtained in the first Se neighbor distances of Zn core are depicted by an upper curve.

in FWHM can only be attributed to the Be-doping induced disorder in the alloy as we have kept constant temperature (room temperature, 300 K) throughout the X-ray absorption spectroscopy. The results of these two composition dependent variants are shown in Figure 7.

Clearly, the composition dependency of $g(r)$ leads to the verdict of large change in the Zn–Se bond lengths on increasing the Be content in the alloy of $\text{Zn}_{1-x}\text{Be}_x\text{Se}$ system. The obtained value of relative bond-length change (ΔL) with respect to equilibrium Zn–Se bonds is found to be 0.02 Å for the alloy composition of 42% Be content $\text{Zn}_{0.58}\text{Be}_{0.42}\text{Se}$. The change indicates towards the increased solid solution hardening of the Zn–Se bonds and thus confirms the alloy hardening as shown in Figure 7(a). It should be noted that the EXAFS measurement errors are by an order magnitude smaller than the measured compositional dependent bond-length contrasts, which are also depicted through the error bars in Figure 7. Surprisingly, during the initial stages of alloying and with the addition of Be, particularly, in the alloy sample B with Be content of 16% we have found the solid solution softening instead of hardening. However, the average bond variations for sample A and C are almost equal. Hence, initially the bond-length contrasts show a flip-flop behavior arising from the crossover in soft-hard bond nature, which can be ascribed to iconicity-induced various competing relaxations processes of mechanical instabilities and frustrations present in the alloy, which gets stabilized by high values of Be content. With a careful comparison of values of the disorder at different compositions, we have also found

an increase of 0.05 Å corresponding to the first shell peaks that show the increase of disorder with alloying in Figure 7(b). The disorder increases to a maximum value of 0.41 Å at the 27% Be concentrations from the initial value of 0.36 Å and surprisingly the disorder decreases thereafter again to the similar value of 0.36 Å at higher Be content of 42% in the sample E. Such an anomalous behavior indicates towards an alloying phenomenon in which the $\text{Zn}_{1-x}\text{Be}_x\text{Se}$ system first becomes fully disordered at the threshold Be concentration of 27%. This composition has the largest variations in the single Zn–Se bond-length distributions with signatures of the presence of multimodal behavior of this bond. Surprisingly, for the same range concentrations (16% to 27%) from Figure 7(a) we have also found the small variations in the ZnSe bond lengths. Hence using these two competitive effects we can attribute that the disorder in this state originates due to some pseudo-crystal stabilities given by the fact that both Be–Se and Zn–Se bonds strive to preserve their original identities and bond lengths. Hence we have obtained the maximum disorder and minimum change in the respective bond lengths for this compositional state. Consequently, we propose that Be content range of 16%–27% is the most favorable alloy composition range for the presence of multimodal or 1-bond-2-mode behaviors for Zn–Se bonds. Nevertheless, on further increasing the Be concentrations, we have found decrease in the disorder parameter and a minima is obtained in the sample E at 42% of Be, implying the total annihilation of alloying related multimodal bond effects. From these results we can understand that the pseudo crystal stability that is one of the main factors for preventing the solid solution hardening gets disturbed at higher Be concentrations and it is manifested by the reduced values of disorder. For that reason, we have obtained a clear trend of gradual increase in the solid solution hardening for alloys with Be concentrations greater than 27%. Lastly, it is a good proposition to incorporate Se-edge EXAFS in the study of ZnBeSe alloys. The atomic environ around Se could provide a more direct picture of the compositional-related changes and that could be a rightful expansion of the present analysis.

4. Conclusion

The synchrotron EXAFS spectroscopy and the various types of data processing and transformations are discussed in this paper with the help of suitable schematics. We have successfully extracted the useful EXAFS oscillations by a careful elimination of the redundant spectrum segments. The comparison among the EXAFS spectroscopy signals is made in normalized energy-space along with extracted modulations in the R- and k-spaces for better understanding of local environs of the core excitation of zinc atom in the compositionally vivid $\text{Zn}_{1-x}\text{Be}_x\text{Se}$ lattice. All the extracted results in various spaces are suitably forward and backward transformed by using apt filter windows for obtaining first shell (NN) and second shell (NNN) distances in respect to the zinc core. Secondly, with the aid of modern ab initio codes the theoretical EXAFS oscillations in various spaces are simulated and fitted with total experimental EXAFS for

attaining oscillatory amplitude contributions from various single and multiple X-ray scattering paths. Significant composition dependent variations in the disorder and the single scattering path length parameter have been obtained on increasing the values of the “ x ” in the range of 0.06 to 0.42 and various steps of parametric evaluation are duly accredited in the paper. Following the parametric extraction, we have studied the bond-length distributions and relative changes in the ZnSe bond-length. Our results point in general towards the solid solution hardening of the alloy with increasing Be concentration and more specifically they describe the presence of multimodal ZnSe bond-length behavior in the specific composition range of $\text{Zn}_{84-73}\text{Be}_{16-27}\text{Se}$. The Zn–Se bond disorder after the threshold concentration of 27% is found to decrease and attains a minimum at 47%. The as-obtained contradictory trends are explained by the presence of the as-found pseudo crystalline stability just before the threshold concentrations, that arises from various competitive processes of bond relaxation. The prospects of suitability of as-hardened ZBS alloy for optoelectronics applications are also discussed.

Acknowledgment

Beamline staff, Synchrotron SOLEIL, are gratefully acknowledged for their help in the EXAFS measurements under the Project CEFIPRA-3204-1.

References

- [1] A. Pawlis, M. Panfilova, K. Sanaka et al., “Low-threshold ZnSe microdisk laser based on fluorine impurity bound-exciton transitions,” *Microelectronics Journal*, vol. 40, no. 2, pp. 256–258, 2009.
- [2] L. S. D. Santos, W. G. Schmidt, and E. Rauls, “Group-VII point defects in ZnSe,” *Physical Review B*, vol. 84, Article ID 115201, 2011.
- [3] A. Toda, F. Nakamura, K. Yanashima, and A. Ishibashi, “Blue-green laser diode grown by photo-assisted MOCVD,” *Journal of Crystal Growth*, vol. 170, no. 1–4, pp. 461–466, 1997.
- [4] M. U. Ahmed, S. J. C. Irvine, A. Stafford, L. M. Smith, A. C. Jones, and S. A. Rushworth, “Decomposition behaviour of nitrogen precursors for p-type doping of pyrolytic and photoassisted MOVPE of ZnSe,” *Journal of Crystal Growth*, vol. 180, no. 2, pp. 167–176, 1997.
- [5] J. I. Kasai, R. Akimoto, T. Hasama et al., “Green-to-yellow continuous-wave operation of BeZnCdSe quantum-well laser diodes at room temperature,” *Applied Physics Express*, vol. 4, Article ID 082102, 3 pages, 2011.
- [6] L. Worschech, W. Ossau, H. J. Lugauer, T. Behr, A. Waag, and G. Landwehr, “ $\langle 110 \rangle$ -uniaxial local strain in epitaxially grown ZnSe on (001)-oriented GaAs,” *Journal of Crystal Growth*, vol. 184–185, pp. 500–504, 1998.
- [7] A. Berghout, A. Zaoui, J. Hugel, and M. Ferhat, “First-principles study of the energy-gap composition dependence of $\text{Zn}_{1-x}\text{Be}_x\text{Se}$ ternary alloys,” *Physical Review B*, vol. 75, no. 20, Article ID 205112, 2007.
- [8] D. O. Dumcenco, C. T. Huang, Y. S. Huang et al., “Optical characterization of $\text{Zn}_{0.95-x}\text{Be}_x\text{Mn}_{0.05}\text{Se}$ mixed crystals,” *Physical Review B*, vol. 79, no. 23, Article ID 235209, 2009.
- [9] F. Plazaola, J. Flyktman, K. Saarinen et al., “Defect characterization of ZnBeSe solid solutions by means of positron annihilation and photoluminescence techniques,” *Journal of Applied Physics*, vol. 94, no. 3, pp. 1647–1653, 2003.
- [10] O. Pagès, A. V. Postnikov, M. Kassem, A. Chafi, A. Nassour, and S. Doyen, “Unification of the phonon mode behavior in semiconductor alloys: theory and ab initio calculations,” *Physical Review B*, vol. 77, no. 12, Article ID 125208, 2008.
- [11] T. Ganguli, J. Mazher, A. Polian, S. K. Deb, O. Pages, and F. Firszt, “An EXAFS study of the structure of the $\text{Zn}_{1-x}\text{Be}_x\text{Se}$ alloy system,” *Journal of Physics: Conference Series*, vol. 190, Article ID 012064, 2009.
- [12] T. Ganguli, J. Mazher, A. Polian et al., “Lattice relaxation in the highly-contrasted $\text{Zn}_{1-x}\text{Be}_x\text{Se}$ alloy: an extended x-ray absorption fine structure study,” *Journal of Applied Physics*, vol. 108, no. 8, Article ID 083539, 2010.
- [13] J. Zakrzewski, M. Maliński, M. Pawlak et al., “Determination of the thermophysical parameters of $\text{Zn}_{1-x}\text{Be}_x\text{Se}$ mixed crystals by means of photothermal techniques,” *Physica Status Solidi (C)*, vol. 3, no. 4, pp. 746–749, 2006.
- [14] M. Maliński, L. Chrobak, J. Zakrzewski, and K. Strzałkowski, “Photoacoustic method of determination of quantum efficiency of luminescence in Mn^{2+} ions in $\text{Zn}_{1-x-y}\text{Be}_x\text{Mn}_y\text{Se}$ crystals,” *Opto-Electronics Review*, vol. 19, no. 2, pp. 183–188, 2011.
- [15] ODE beamline, 2007, <http://www.synchrotron-soleil.fr/Recherche/LignesLumiere/ODE>.
- [16] F. Baudelet, Q. Kong, L. Nataf et al., “ODE: a new beam line for high-pressure XAS and XMCD studies at SOLEIL,” *High Pressure Research*, vol. 31, no. 1, pp. 136–139, 2011.
- [17] B. Ravel and M. Newville, “ATHENA, ARTEMIS, HEPHAESTUS: data analysis for X-ray absorption spectroscopy using IFEFFIT,” *Journal of Synchrotron Radiation*, vol. 12, no. 4, pp. 537–541, 2005.
- [18] P. A. Lee, P. H. Citrin, P. Eisenberger, and B. M. Kincaid, “Extended x-ray absorption fine structure—its strengths and limitations as a structural tool,” *Reviews of Modern Physics*, vol. 53, no. 4, pp. 769–806, 1981.
- [19] D. E. Sayers and B. Bunker, “Data analysis,” in *X-Ray Absorption: Principles, Applications, Techniques of EXAFS, SEXAFS, and XANES*, D. C. Koningsberger and R. Prins, Eds., p. 216, Wiley, New York, NY, USA, 1988.
- [20] IFEFFIT Documentation, 2010, <http://cars9.uchicago.edu/ifeffit>.
- [21] J. J. Rehr, R. C. Albers, C. R. Natoli, and E. A. Stern, “New high-energy approximation for x-ray-absorption near-edge structure,” *Physical Review B*, vol. 34, no. 6, pp. 4350–4353, 1986.
- [22] G. M. Bhalerao, A. Polian, M. Gauthier et al., “High pressure x-ray diffraction and extended x-ray absorption fine structure studies on ternary alloy $\text{Zn}_{1-x}\text{Be}_x\text{Se}$,” *Journal of Applied Physics*, vol. 108, no. 8, Article ID 083533, 2010.



Hindawi

Submit your manuscripts at
<http://www.hindawi.com>

